A Robotic System for Transanal Endoscopic Microsurgery: Design, Dexterity Optimization and Prototyping

Jichen Li, Shuxin Wang, Zhiqiang Zhang, Chaoyang Shi

***Abstract*—This paper proposes a master-slave operated robotic system that features the novel slave manipulator with a modular distal continuum section to address the shortcomings of traditional transanal endoscopic microsurgery (TEM). The slave manipulator consists of two 7-DoF surgical instruments and a 5-DoF endoscopic arm that are designed with distal continuum structures and unfolded with a Y configuration after inserting through a transanal port to enhance hand-eye coordination and instrument triangulation. The proposed robot is designed for adaptation in narrow and shallow rectal spaces, facilitating intuitive hand-eye coordination and enhanced operational dexterity with reduced obstruction of the field of view. A novel hybrid coaxial continuum unit (HCCU) has been designed to offer excellent bending characteristics and structural stiffness. This unit has been developed as a modular design and supports different connection configurations to form the multi-DoF surgical instruments and endoscopic arm. FEA-based structure optimization has been implemented to improve the mechanical performances of the HCCU unit. Dexterity optimization under anatomical constraints is proposed to improve the maneuverability of the multi-DoF distal continuum section. Experimental investigations on bending and anti-twisting performances on the designed HCCU joint are carried out. The average error value of distal positioning within [-100°, 100°] does not exceed 1.10%, and the torsional stiffness is 6.86 mNm/°. The payload capability of the surgical instrument has been investigated to demonstrate a maximum value of 5 N. The robotic system is prototyped and the trajectory tracking experiments have been performed to validate its positioning accuracy. The user study has been investigated, and the simulated operation tasks that include grape peeling and suturing operations as well as apricot suturing and threading operations, have been performed. The experimental results demonstrate its potential to be utilized in TEM surgery with an extensive surgical field of view and excellent maneuverability.**

***Index Terms*— Transanal endoscopic microscopy, surgical robotics, single-port surgery, flexible endoscopy, continuum manipulator, design optimization, dexterity optimization.**

I. Introduction

As the third most common malignant neoplasm worldwide, colorectal cancer (CRC) has become a significant health problem. With population growth and aging, rectal cancer deaths are projected to rise by 71.5% worldwide until 2035 [1]. Transanal endoscopic microsurgery (TEM), which was developed by Buess in the early 1980s [2], has been popularly introduced as an emerging procedure to remove early rectal cancers and polyps in a minimally invasive surgical manner. The typical TEM is essentially a single-port surgery (SPS) procedure and utilizes two rigid handheld instruments with an X configuration and a stereoscope operating through a transanal port [3]. Compared with conventional techniques, TEM avoids skin incisions, provides a better field of view with stereoscopic vision, and significantly reduces the probability of complications. Although appealing, TEM still lacks instrument triangulation due to narrow operating space and suffers from limited flexibility owing to the rigid instruments and the mirrored and unintuitive hand-eye coordination by the fulcrum effect [4]. These problems have led to limited operational dexterity, flexibility and precision, probable misconduct, and a steep learning curve, which limits the rapid development of the TEM procedure. To address these challenges, several robotic systems have been developed in two typical categories: the general-purpose robotic system for single-port surgery and the specialized surgical robots for TEM.

The general-purpose robotic SPS systems include the commercial products of da Vinci SP [5] by Intuitive Surgical Inc (Sunnyvale, USA), and ongoing developed systems such as SPRINT [6], IREP [7], SHURUI [8], and SPS [9] platform. These robotic systems typically consist of 2 or 3 multi-DoF surgical instruments and a stereo endoscope. These devices are designed based on highly articulated joints or flexible continuum structures. After being inserted through a central port, they are deployed with the Y-shape configuration to provide operational triangulation with a stereoscopic vision [10], [11]. However, most of them are designed for intra-abdominal surgery within large workspaces, resulting in relatively large sizes, lengthy joints, and unoptimized designs for the narrow and restricted rectal cavity environment.

New attempts have also been made to develop specialized surgical robots to tackle TEM in the narrow and confined rectal environment. Hamlyn Center in Imperial College London

Manuscript received Feb. 5th, 2023. This work is supported in part by National Natural Science Foundation of China under Grant 92148201, Grant 51721003, Grant 62211530111, Royal Society under IEC\NSFC\211360, and Graduate research innovation project by Tianjin Education Commission under Grant 2022BKY075. *(Corresponding author: C. Shi)*

Jichen Li is a PhD student with the School of Mechanical Engineering, Tianjin University, Tianjin, 300072, China (e-mail: lijichen@tju.edu.cn).

Shuxin Wang is a Professor with the School of Mechanical Engineering, Tianjin University, Tianjin, 300072, China. He was elected as an Academician of the Chinese Academy of Engineering (e-mail: shuxinw@tju.edu.cn).

Zhiqiang Zhang is an Associate Professor with the University of Leeds, Leeds, LS2 9JT, UK (e-mail: z.zhang3@leeds.ac.uk).

Chaoyang Shi is a Professor with the School of Mechanical Engineering, Tianjin University, Tianjin, 300072, China (e-mail: chaoyang.shi@tju.edu.cn).

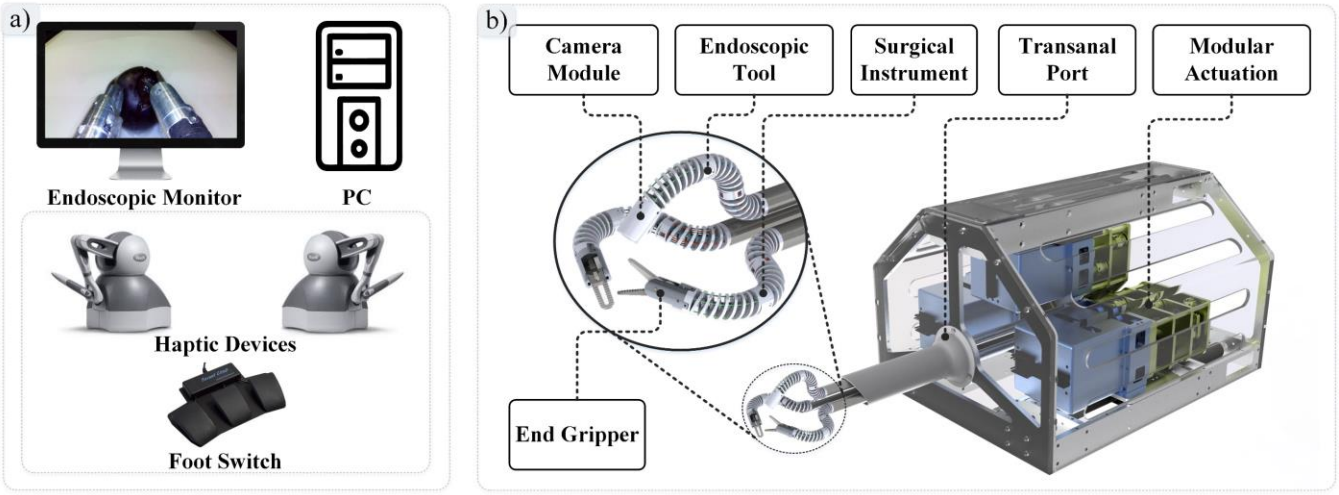

Fig. 1. Main components of the TEM robotic system. a) The master console with two haptic devices and a foot switch. b) The slave manipulator consisting of a 5-DoF endoscopic tool, two 7-DoF surgical instruments, a transanal port and a modular actuation unit.

developed the micro-IGES system with two successive versions [12]. The first-version robotic slave system has two 7-DoF surgical instruments for operations and a 3D commercial endoscope to provide imaging and has been experimentally validated. However, the surgical instrument comprises articulated joints produced by stainless steel additive manufacturing [13]. Due to the high friction and bending discontinuities, this design suffered from nonlinear transmission and low motion accuracy problems, which require additional compensation. In addition, the lack of an adjustable structure for the commercial endoscope resulted in its position being close to the instrument shaft, severely obscuring the surgical field of view. To solve the problems caused by the articulated joints, Hu et al. have developed a TEM robotic system based on continuum joint design [14]. It consists of two 5-DoF surgical instruments and a 4-DoF endoscope. The instrument adopted a two-section continuum joint with a distal suturing tool and is capable of positioning, suturing, and knotting in the rectal cavity. However, each section of the continuum joints has only 1 DoF and needs further optimization to enhance flexibility. In addition, these two systems adopt the overall rotation of the instrument (Base Rot) rather than the distal rotation (Wrist Rot), which needs to be further improved to enhance maneuverability.

To further upgrade the operating environment for the robot-assisted TEM procedures, this work presents a novel robotic system based on modular continuum joints for adaptation in narrow and shallow rectal spaces, which supports intuitive hand-eye coordination, comfortable operating triangulation, and enhanced operational dexterity with reduced obstruction of the field of view. The distal multi-DoF continuum section mainly comprises a series of hybrid coaxial continuum units (HCCU), which feature a trade-off between excellent bending characteristics and structural stiffness. The specially designed proximal continuum segment and particular tendon/rod arrangement support the decoupling of structure position and orientation, simplifying the closed-form kinematic solution and reducing the control complexity. A two-step design optimization methodology, including structure and kinematic optimization, has been presented and implemented. Structure optimization has been performed to improve the performances of the HCCU unit, and the kinematic optimization under narrow anatomical constraints has been performed to enhance the operational dexterity of the multi-DoF continuum section. Bending and torsion performance evaluations of the HCCU joint have been performed. The proposed design targets a more narrow and shallow rectal space via the natural anal opening for the TEM procedures rather than the general multi-arm single port system for laparoscopic and thoracic surgery. In addition, the traditional SPS robots typically combine the proximal joint-based part and distal continuum design-based part as the surgical instruments to yield a large workspace and proper dexterity. In contrast, the proposed robot adopts a hybrid continuum unit design, offering excellent bending properties and dexterity, favorable compliance, and modular expansion capability. The robotic system has been prototyped, and the loading capability and simulation tasks have also been further investigated to validate its effectiveness.

II. Materials and Methods

A. Design Specifications of the TEM Robotic System

The robot-assisted TEM procedures are required to provide surgeons with an upgraded operating environment that offers improved triangulation, intuitive hand-eye coordination, and enhanced dexterity to tackle the issues in the traditional TEM procedures and further enhance patient treatment outcomes. The detailed design specifications for the robotic TEM systems are listed as follows: (1) The outer diameter of the robot is acceptable at less than 40mm to pass through a transanal port in a parallel state [3]. (2) The robot typically includes two flexible operational instruments that are designed with not less than five DoFs to deploy within the body to form an operational triangulation and could be replaced and exchanged when necessary. The outer diameter of each instrument is acceptable at no more than 12mm [12], [14]. (3) The load capability of each instrument is typically not less than 2N to sufficiently

perform operations such as pulling and peeling of the tissue [8]. (4) Considering the rectum's physiological size, the robot's workspace is ideally larger than 35mm×35mm×60mm [4]. (5) The robot is required to be equipped with an illuminated section that contains an imaging endoscope, typically featuring no fewer than three DoFs.

B. Overview of the Proposed Robotic System

The overview of the proposed TEM robotic system with a master-slave configuration has been illustrated in Fig. 1. The master console consists of two haptic devices, a foot switch, an HD endoscopic monitor, and a host PC (Fig. 1a)). The slave manipulator consists of three functional tools including a 5-DoF endoscope, two 7-DoF surgical instruments, a transanal port for insertion into the patient's rectum, and a modular actuation unit, as shown in Fig. 1b). The surgical instrument and endoscope adopt the same design scheme that utilizes a multi-DoF distal continuum section consisting of three HCCUs with different connection configurations. The transanal port is 32 mm in diameter and consists of three parallelly aligned channels to carry the endoscope and designed instruments. The surgical instruments enter the rectum through the two lower channels and unfold to form a dual-armed working configuration. The endoscope is assembled inside the upper channel for imaging guidance.

C. Design of the Multi-DoF Distal Continuum Section for the Surgical Instruments and Endoscope

1) Hybrid coaxial continuum unit (HCCU) design concept

TABLE I
INITIAL DESIGN PARAMETERS OF THE HCCU UNIT

Symbol	Description
p	Pitch of the helical structure [mm]
w	Width of the helical cross section [mm]
b	Height of the helical cross section [mm]
D_1	Diameter of internal channel [mm]
D_2	Outer diameter of the hollow tube [mm]
D_3	Moment arm of the driving cable [mm]
D_4	Outer diameter of the helical structure [mm]
n	Coil number
l	Effective bending length of the HCCU [mm]
h_1	Outer height of the notch [mm]
h_2	Inside height of the notch [mm]
ω_1	Width of the notch [mm]
ω_2	Depth of the notch [mm]
ω_3	Ratio of ω_2 to D_1
θ	Bending angle [rad]

The proposed novel HCCU unit primarily consists of an outside dual-helix structure with a rectangular cross-section and a notched central backbone, and they are coaxially arranged and manufactured by 3D printing, as shown in Fig. 2a). It has been developed as a modular design to form the multi-DoF distal continuum section of surgical instruments and endoscope. This helix-based continuum joint offers excellent bending properties and favorable compliance, achieving bending motion with two DoFs. The stress is uniformly distributed on the helical structure in the bending process, and the total structural length to bear the stress is longer than the other types of flexible joints. These features lead to reduced stress concentration, outstanding constant bending curvature characteristics, and improved bending repeatability. Besides, compared with the standard single-helix structure, the proposed dual-helix structure can depress the force-induced length variation and improve the torsional stiffness. To further improve the anti-twisting and load capability, the notched central backbone with a hollow center is introduced and designed coaxially inside the dual-helix structure. The designed built-in central backbone can effectively improve compressive stiffness without sacrificing the bending properties of the outer dual-helix structure.

Connecting interfaces are configured at both ends of the HCCU to facilitate the modular segments stacking and form a multi-DoF distal continuum joint section. Compared with other flexible joints such as [15]–[17], HCCU shows excellent comprehensive performances and empowers wiring and tool passing via the hollow center. In addition, this unit offers excellent stability, a large workspace, and modular expandability of integration for surgical instruments. The HCCU unit is manufactured with nylon material (Young's modulus of 1200 MPa and yield strength of 48 MPa) by the fused layer manufacturing process. The detailed dimensional parameters and their description have been listed in Table I.

2) Structural parameter optimization based on FEA

To balance the trade-off between the flexibility and stiffness of a single-section continuum joint, the critical design variables of the HCCU unit are optimized based on FEA via ANSYS Workbench 2020 (ANSYS Inc., Pennsylvania, USA). The parametric geometry model of the HCCU unit is generated using Solidworks and subsequently imported into ANSYS Workbench. The torsional moments, compression forces, and bending moments can be configured with parameter settings in the "Static Structural" module. They are applied to the parametric model of HCCU for simulation investigation, as shown in Fig. 2b). The simulation settings have been detailed in Appendix. A. The applied loads and the corresponding deflections are collected, and the equivalent mechanical properties independent of length are defined as

$$\tilde{T} = \frac{M_t l}{D_t}, \tilde{C} = \frac{F_C l}{D_c}, \tilde{B} = \frac{D_b}{M_b l}, \quad (1)$$

where, $\tilde{T}$, $\tilde{C}$ and $\tilde{B}$ represent the equivalent torsional stiffness, compression stiffness, and bending flexibility, respectively. M_t, F_C and M_b denote the loads applied in the three simulations. D_t, D_c and D_b represent the maximum values of total deformation for the mesh elements in FEM that correspond to the torsional, compression, and bending loading, respectively. l expresses the effective length of the HCCU. It is calculated by $l = np$, and the coil number n is set to 4.

The optimization of the parameters aims to improve the bending flexibility while reducing the deformation subjected to compression and the torsional load. It can be described as

$$\max \boldsymbol{F}(\boldsymbol{X}) = \left[\tilde{T}(X)\ \tilde{C}(X)\ \tilde{B}(X)\right],\ \ \boldsymbol{X} = [p, b, D_2, h_1, \omega_3]^T$$

$$\text{subject to} \begin{cases} 4\ \text{mm} \le p \le 8\ \text{mm} \\ 0.5\ \text{mm} \le b \le 2\ \text{mm} \\ 2\ \text{mm} \le D_2 \le 4\ \text{mm} \\ 0.5\ \text{mm} \le h_1 \le 2.5\ \text{mm} \\ 0.5 \le \omega_3 \le 1 \end{cases}, \quad (2)$$

where $\boldsymbol{X}$ is the design variables vector. The variation ranges of the critical variables are described as a set of constraints based on the manufacturing constraints and the intrinsic geometric requirements.

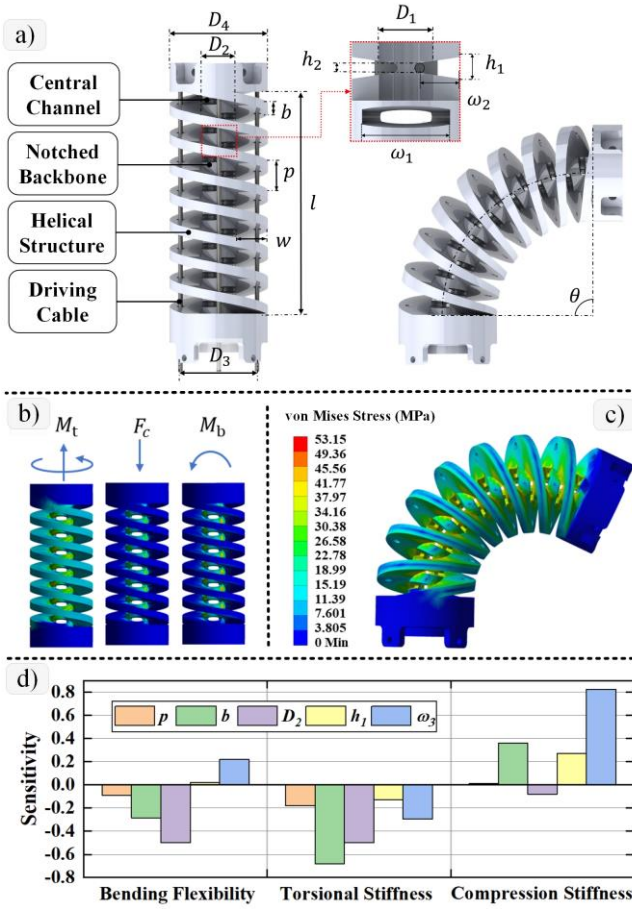

Fig. 2. a) Detailed structure of the HCCU unit. b) Load settings for each FEA simulation. c) The FEA results of von Mises stress distribution for the optimized HCCU structure. d) Contribution of the design variables on the objective function based on the built - in sensitivity analysis.

To speed up the calculation, HCCU is assumed to work in the linear elastic stage and exhibit uniformly distributed stiffness properties along the axial direction. The built-in sensitivity analysis function is further performed to evaluate the influences of design variables on the objective function and simplify the subsequent optimization with reduced variables. The results of the sensitivity analysis fall within the range of [-1, 1], in which the larger absolute values indicate a more significant impact on objective functions, and the sign denotes a positive/negative contribution to the objective function. As determined in Fig. 2d), p and h_1 characterize smaller sensitivity values and make fewer contributions. Therefore, they are configured with constants $p = 6$ mm, $h_1 = 2.3$ mm. Considering the manufacturing constraints and rectal size constraints, the diameter of the central channel D_1 is set to 1.7 mm to pass through a flexible shaft with a diameter of 1.5 mm, while the outer diameter D_4 is set to 10 mm.

Subsequently, the built-in multi-objective genetic algorithm in the "Response Surface Optimization" module was applied to determine the optimal solutions due to its high search effectiveness for global optimization, as summarized in Table II. The static performance analysis of the optimized design was performed, as illustrated in Fig. 2c). The HCCU exhibits a large bending angle and excellent constant curvature characteristics. The equivalent stress is uniformly distributed over the notched backbone and the helical structure when the bending moment is applied to the HCCU.

TABLE II
COMPARISON OF THE DETAILED STRUCTURAL PARAMETERS BEFORE AND AFTER OPTIMIZATION

	b(mm)	D_2(mm)	ω_3
Initial value	1.00	4.00	0.80
Final value	1.21	3.42	0.64

3) Design of the multi-DoF continuum section based on the HCCU unit

To improve the operational triangulation in the narrow rectum, a proximal associated continuum segment (PACS) is proposed, which consists of a stack of two HCCU joints, termed as the active segment (AS) and the passive segment (PS), as shown in Fig. 3a). The driving tendons are specifically arranged so that the PACS performs an S-shape to achieve the parallel relationship between its distal end plane and the proximal base. The AS segment adopts the active wire-driven approach, and the tendons (OD=0.45 mm, made by tungsten alloy) are fixed in the intermediate rigid connection part and are pulled by the driving unit. In contrast, the PS segment utilizes the passive rod-driven approach by employing four nitinol rods (OD=0.5 mm). This is attributed to their high axial stiffness and incompressibility during the pulling and pushing process, which eliminates the need for pre-tensioning. In addition, the incorporation of nitinol rods can further enhance the proximal load capability. The two ends of the rods are attached to the base of the AS and the tip of the PS. Therefore, when actively bending the AS, the rods inside the PS are constrained and their length remains constant, leading to the PS producing an equivalent bending motion in the opposite direction. The PACS section will maintain an S-shape, ensuring that the orientation of the PS distal end remains parallel to the base at all times. This design reduces the number of driving units required for multi-DoF instruments.

A continuum section with a deployable function is further proposed, and it mainly consists of a single HCCU unit as a distal segment (DS) and a PACS part, as shown in Fig. 3b). The DS generates a 2-DoF bending along the $\hat{\boldsymbol{x}}$ and $\hat{\boldsymbol{y}}$ directions. The tendons (OD=0.45 mm, made by tungsten alloy) of DS are arranged on the medial circumference through the entire PACS. The distribution locations and lengths for the driving wires of the AS and DS segments and the passive rods of the PS segment

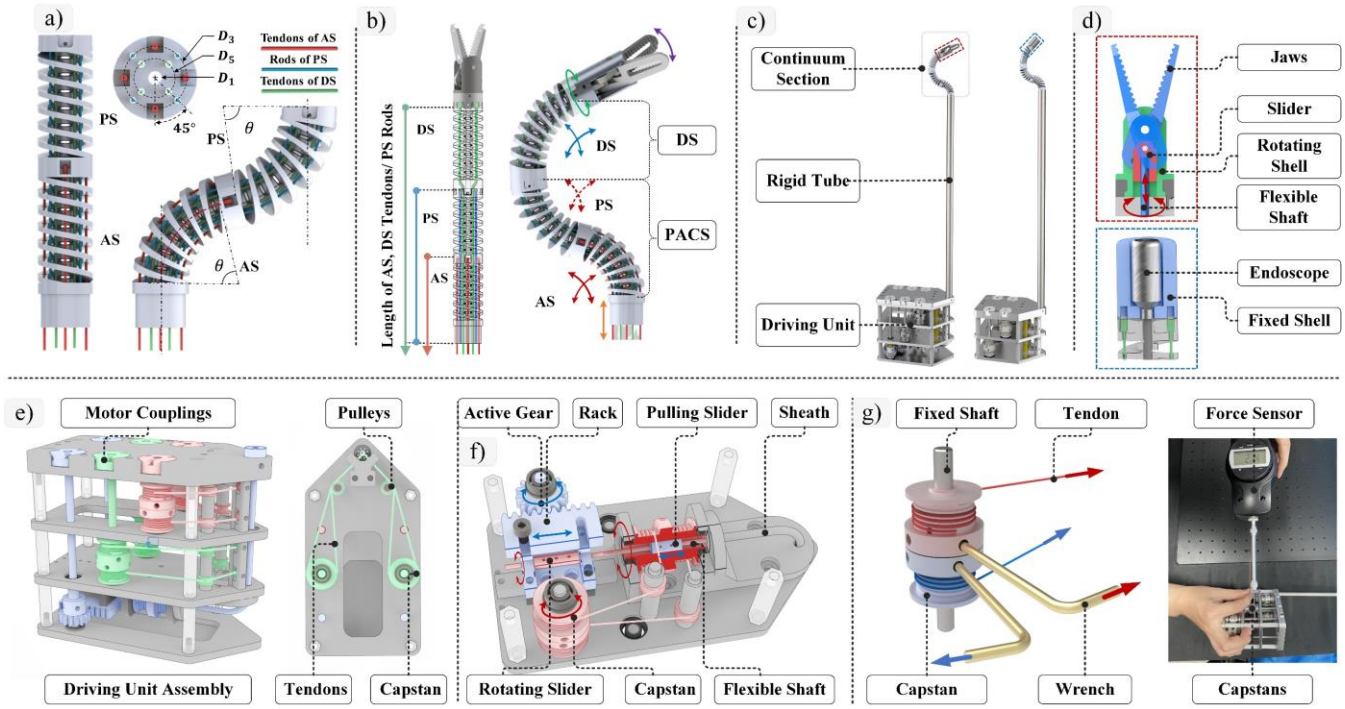

Fig. 3. a) Design concept of the proposed proximal associated continuum segment (PACS). b) Design of the multi-DoF continuum section. c) Design of surgical instrument and endoscopic tool. d) Design of the end gripper and endoscope module. e) Driving unit assembly of the surgical instruments. f) Working principle of the driving layer 3 for flexible shaft. g) The process of the pre-tension application on tendons.

have been labeled in Fig.3a)-b) for better illustration. Due to the S-shaped configuration of PACS, the length of the DS tendons within the proximal segment remains constant. As a result, the orientation of DS is theoretically unaffected by PACS, simplifying the kinematic solution and reducing the control complexity. In contrast with the conventional multi-segment continuum joint design, the configuration of tendons and rods proposed in this paper effectively achieves motion decoupling between the distal and proximal segments without requiring additional consideration of tendons' routing for the distal segment. The details of the PACS section's bending and motion decoupling performances have been demonstrated in the Appendix. B.

D. Assembly of the Surgical Instruments and Endoscope

Both surgical instruments and endoscopic tools consist of three parts: a distal multi-DoF continuum section, a middle connection tube, and a proximal driving unit, as shown in Fig.3c). This multi-segment continuum joint can be customized for different surgical scenarios [18] to overcome the limitations of the intrinsic space constraints due to its excellent extensibility. For surgical instruments, a flexible shaft is selected to drive the rotation and clamping of the end gripper due to the ability to transmit thrust, tension, and torque, as shown in Fig. 3d). The utilized flexible shaft (MAISO, CN) is made of 304 stainless steels with a diameter of 1.5 mm and a total length of 580 mm. It provides a relatively large torsional stiffness value of 0.135 mNm/°, supporting effective torque transmission to enable the distal rotation of the gripper. Besides, the bending stiffness of the flexible shaft was measured as 0.105 N/mm by the typical three-point bending flexural test, which slightly affects the bending motion performance of the HCCU joint. For the endoscope, a CMOS module with an outer diameter of 5.5 mm is attached to the end of the endoscope to provide visual information. The detailed design of the driving unit is shown in Fig. 3e). The driving tendons and the flexible shaft are delivered to separate driving layers after passing through a PTFE multi-channel tube. The driving layers 1 and 2 generate antagonistic tendon stretch-contraction motions via capstans to drive DS and PACS. In the driving layer 3 for flexible shaft, as shown in Fig. 3f), a pair of capstans are used to produce the rotary motion, and a rack-and-pinion mechanism is designed to achieve both push and pull motions for the flexible shaft. With this design, the two movements of rotation and translation (pull and push) are appropriately decoupled. Different driving layers share a uniform connection interface to facilitate the rapid replacement of instruments during the operation. Besides, the pre-tension force is applied to each wire-driving tendon (AS and DS) through the specially designed capstans for tendon winding, as shown in Fig. 3g). The wrench can be utilized to apply the pre-tension force on each driving tendon based on the principle of leverage amplification. A force sensor (WDF-30N, WDGAGE, CN) can measure the wrench-applied force, and then the pre-tension force generated on the driving tendon can be calculated. For our experiments, the pre-tension force values were estimated at approximately 14.05 N and 11.5 N for AS and DS tendons, respectively. More manufacturing details have been added in the Appendix. C.

E. Kinematics for the Surgical Instruments

Considering the similarity of the surgical instruments, the forward and closed-form inverse kinematics for surgical

instruments are presented. Fig. 4a)-b) defines the necessary nomenclature and frames that specify the kinematics of the robotic system. The kinematic state of the surgical instrument is determined by the configuration vector $\boldsymbol{\psi_c} = [d, \theta_1, \alpha_1, \theta_2, \alpha_2, \alpha_3]^T$. d indicates the translational length of the instrument. θ_1, α_1 and θ_2, α_2 are the constant curvature model parameters for AS and DS respectively. α_3 represents the rotation angle of the distal end gripper. The homogeneous transform from the frame $\{W\}$ to the frame $\{E\}$ is expressed as follows:

$$ {}^W_E\boldsymbol{T} = {}^W_B\boldsymbol{T}\,{}^B_1\boldsymbol{T}\,{}^1_5\boldsymbol{T}\,{}^5_6\boldsymbol{T}\,{}^6_E\boldsymbol{T} = \begin{bmatrix} {}^W_E\boldsymbol{R} & {}^W_E\boldsymbol{p} \\ \boldsymbol{0}_{1\times3} & 1 \end{bmatrix}, \tag{3} $$

where the base fame $\{B\}$ is derived from the world frame $\{W\}$ by translating a constant position vector ${}^W_B\boldsymbol{p}$. The rigid tube is translated in $\hat{\boldsymbol{z}}_B$ by d, and the operator ${}^B_1\boldsymbol{T}$ is obtained.

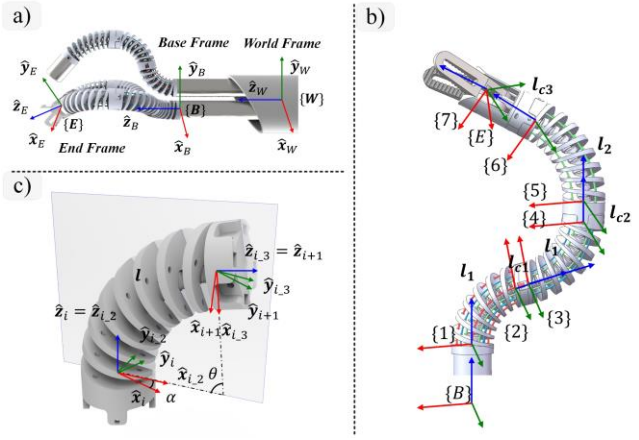

Fig. 4. Nomenclature and frames of a) the transanal port and surgical instruments, b) segments on surgical instrument, and c) the single HCCU segment.

The configuration of the PACS is specified due to $\boldsymbol{\psi_{PACS}} = [\theta_1, \alpha_1]^T$. Based on the constant curvature model shown in Fig. 4c), the translational position vector ${}^1_5\boldsymbol{p}$ of PACS can be calculated as

$$ {}^1_5\boldsymbol{p} = \begin{bmatrix} \frac{2c_{\alpha_1} l_1 (1-c_{\theta_1})}{\theta_1} + l_{c1} c_{\alpha 1} s_{\theta_1} \\ \frac{2s_{\alpha_1} l_1 (1-c_{\theta_1})}{\theta_1} + l_{c1} s_{\alpha 1} s_{\theta_1} \\ \frac{2l_1 s_{\theta_1}}{\theta_1} + l_{c1} c_{\theta_1} + l_{c2} \end{bmatrix}. \tag{4} $$

When $\theta_1 = 0$, thus the translational position vector can be denoted as ${}^1_5\boldsymbol{p} = [0 \quad 0 \quad 2l_1 + l_{c1} + l_{c2}]^T$.

The distal segment is specified by the configuration vector $\boldsymbol{\psi}_{DS} = [\theta_2, \alpha_2]^T$. The homogeneous transform ${}^5_6\boldsymbol{T}$ is

$$ {}^5_6\boldsymbol{T} = \begin{bmatrix} {}^5_6\boldsymbol{R} & {}^5_6\boldsymbol{p} \\ \boldsymbol{0}_{1\times3} & 1 \end{bmatrix}, \tag{5} $$

where

$$ \begin{cases} {}^5_6\boldsymbol{R} = \begin{bmatrix} c_{\theta_2}(c_{\alpha_2})^2 + (s_{\alpha_2})^2 & s_{\alpha_2} c_{\alpha_2}(c_{\theta_2} - 1) & c_{\alpha_2} s_{\theta_2} \\ s_{\alpha_2} c_{\alpha_2}(c_{\theta_2} - 1) & c_{\theta_2}(s_{\alpha_2})^2 + (c_{\alpha_2})^2 & s_{\alpha_2} s_{\theta_2} \\ -c_{\alpha_2} s_{\theta_2} & -s_{\alpha_2} s_{\theta_2} & c_{\theta_2} \end{bmatrix}. \\ {}^5_6\boldsymbol{p} = (l_2/\theta_2)\begin{bmatrix} c_{\alpha_2}(1-c_{\theta_2}) & s_{\alpha_2}(1-c_{\theta_2}) & s_{\theta_2} \end{bmatrix}^T \end{cases} $$

The frame $\{E\}$ is translated l_{c3} relative to frame $\{6\}$ in $\hat{\boldsymbol{z}}_6$ and rotated about $\hat{\boldsymbol{z}}_7$ by α_3. Therefore, the frame defining $\{E\}$ is:

$$ {}^6_E\boldsymbol{T} = trans(\hat{\boldsymbol{z}}_6, l_{c3}) \times rot(\hat{\boldsymbol{z}}_7, \alpha_3) = \begin{bmatrix} {}^6_e\boldsymbol{R} & {}^6_e\boldsymbol{p} \\ 0_{1\times3} & 1 \end{bmatrix}. \tag{6} $$

The inverse kinematics of the surgical tool is derived as follows. Firstly, the orientation of the surgical instruments is determined only by the DS. Namely, ${}^B_E\boldsymbol{R} = {}^5_6\boldsymbol{R}\,{}^6_E\boldsymbol{R}$, and ${}^B_E\boldsymbol{R}$ has the following form:

$$ {}^B_E\boldsymbol{R} = \begin{bmatrix} n_x & a_x & c_{\alpha_2} s_{\theta_2} \\ n_y & a_y & s_{\alpha_2} s_{\theta_2} \\ -c_{\alpha_2 - \theta_3} s_{\theta_2} & -s_{\alpha_2 - \theta_3} s_{\theta_2} & c_{\theta_2} \end{bmatrix}. \tag{7} $$

Equating the above elements, the orientation configuration vector $\boldsymbol{\psi_o} = [\theta_2, \alpha_2, \alpha_3]^T$ can be derived as: $\theta_2 = \text{acos}({}^B_E\boldsymbol{R}_{,33})$, $\alpha_2 = \text{Atan2}({}^B_E\boldsymbol{R}_{,23}, {}^B_E\boldsymbol{R}_{,13})$ and $\alpha_3 = \alpha_2 - \text{Atan2}(-{}^B_E\boldsymbol{R}_{,23}, -{}^B_E\boldsymbol{R}_{,13})$. Subsequently, Eq. (3) can be rewritten as

$$ {}^E_B\boldsymbol{p} = {}^B_5\boldsymbol{p} + {}^5_E\boldsymbol{p} = {}^5_6\boldsymbol{R}\,{}^6_E\boldsymbol{p} + {}^5_6\boldsymbol{p} + {}^B_1\boldsymbol{p} + {}^1_5\boldsymbol{p}\,, \tag{8} $$

where ${}^5_E\boldsymbol{p}$ can be calculated from the configuration vector $\boldsymbol{\psi_o}$. Eventually, the configuration vector $\boldsymbol{\psi_p} = [d \quad \theta_1 \quad \alpha_1]^T$ can be solved numerically. The closed-form inverse kinematic is completely solved.

F. Dexterity Optimization under Anatomically Constrained

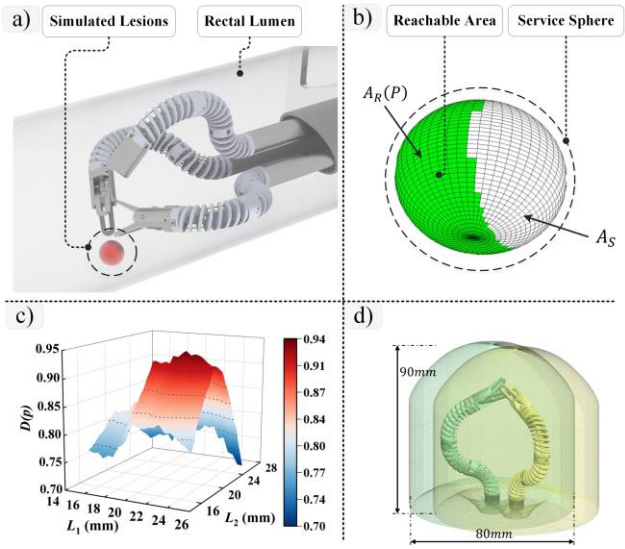

Fig. 5. a) Simplified working scenario of the TEM robotic system. b) Dexterity representation based on service sphere. c) Dexterity optimization results for different segment length configurations. d) The optimized dual-arm instrument workspace.

A customized optimization method is proposed to optimize the operational dexterity of the robot by configuring the AS (equal to PS) and DS lengths. This approach provides an intuitive characterization of dexterity and considers the rectum's anatomical constraints, which can improve the maneuverability of the designed robot in confined spaces.

Firstly, the surgical scenario is appropriately simplified, as shown in Fig. 5a). Taking into account the softness of the intestinal tissue, the rectum is simplified as a 45 mm diameter tube. A simulated lesion is arranged directly below the endoscopic field of view. This is because surgeons generally position the patient appropriately so that the lesion is always located in a lower part of the surgical area in conventional TEM surgery.

The dexterity stereo angle approach was used as an evaluation index to measure the operational dexterity of the TEM robot, as shown in Fig 5b). Compared with the manipulability index based on the Jacobian matrix condition number, the dexterity stereo angle based on orientability is more geometrically intuitive, which can be described as:

$$D_P = \frac{A_R(P)}{A_S} = \frac{N_O(P)}{N_\theta N_h} \in (0,1], \tag{9}$$

where $A_R(P)$ denotes the area of the service area at position P and A_S is the total surface area of the service sphere. The service sphere is uniformly divided into $N_\theta \times N_h$ patches, and the area of each patch is equal. N_θ and N_h denote the number of longitudinal and latitudinal lines, respectively. The dexterity D_P can be calculated as the ratio of patches reached by the $N_O(P)$ over the total number of patches $N_\theta N_h$. Thus, the parameter selection is transformed into an optimization problem that can be described as:

$$Z = \max[D_P(\boldsymbol{X}) + \eta(\boldsymbol{X})], \boldsymbol{X} = [l_1, l_2, d, \theta_{1\max}, \theta_{2\max}]^T$$

$$\textbf{subject to} \begin{cases} 0 \le l_1 \le 40 \text{ mm} \\ 0 \le l_2 \le 40 \text{ mm} \\ 10 \text{ mm} \le d \le 25 \text{ mm}, \\ 0 \le \theta_{1\max} \le l_1 k \\ 0 \le \theta_{2\max} \le l_2 k \end{cases} \tag{10}$$

where $D_P(\boldsymbol{X})$ represents the service surface dexterity of the surgical instrument in the simulated lesion region. To avoid the decrease in instrument stiffness, a constraint on the total length of the instrument is required. $\eta(\boldsymbol{X})$ is introduced as a normalized expression of the total length, $\eta(\boldsymbol{X}) = 1 - (l_1 + l_2)/80 \in (0,1]$. $\boldsymbol{X}$ is defined as a vector representing the structural variables with joint constraints $\boldsymbol{X} = [l_1, l_2, d, \theta_{1\max}, \theta_{2\max}]^T$. The bending angle constraints of joint variables θ_1 and θ_2 are varied with the lengths of l_1 and l_2. According to the FEA results, the constraint is set to $0 \le \theta_{\max} \le lk$, where $k = 0.08$.

The optimization process is detailed as follows: (1) arrange the combination l_1, l_2 at a 0.5 mm interval to generate the experimental dataset and determine $\eta(\boldsymbol{X})$. (2) determine the homogeneous transformation matrix ${}^W_E\boldsymbol{T}_{\text{given}}$ with position $\boldsymbol{p} = [0, -16, 60]^T$, and the orientation is generated through the service sphere represented as a binary matrix of $N_\theta N_h = 20 \times 10$. (3) input the ${}^W_E\boldsymbol{T}_{\text{given}}$ to the derived inverse kinematics. The algorithm is solved for the configuration vector $\boldsymbol{\psi}$ and the end of PACS position vector $\boldsymbol{p}_5^W$. If the numerical solution can be obtained without exceeding the limit of each joint and the $\boldsymbol{p}_5^W$ does not extend beyond the rectal lumen then $N_O(P)$ is added 1, otherwise $N_O(P)$ remains unchanged. (4) the dexterity D_P for various configurations of l_1, l_2 are obtained by Formula (9), and $Z \in (0,2]$ is obtained after accumulating with $\eta(\boldsymbol{X})$ and plotted.

The optimization results are illustrated in Fig. 5c). It can be seen that the performance of the instrument is optimized when $l_1 = 20.5$ mm, $l_2 = 23$ mm, and the dexterity $D_P = 0.532$. The optimized dual-arm instrument workspace has been determined, as shown in Fig. 5d). The single instrument workspace forms an ellipsoidal shape of 80 mm in diameter and 90 mm in length, and the overlapped workspace of the dual instruments outlines a cylinder of 40 mm. This working area is sufficient to cover the entire rectum and meet the surgical requirements of TEM.

III. Experiments and Results

A. Hardware Configuration of the Proposed System

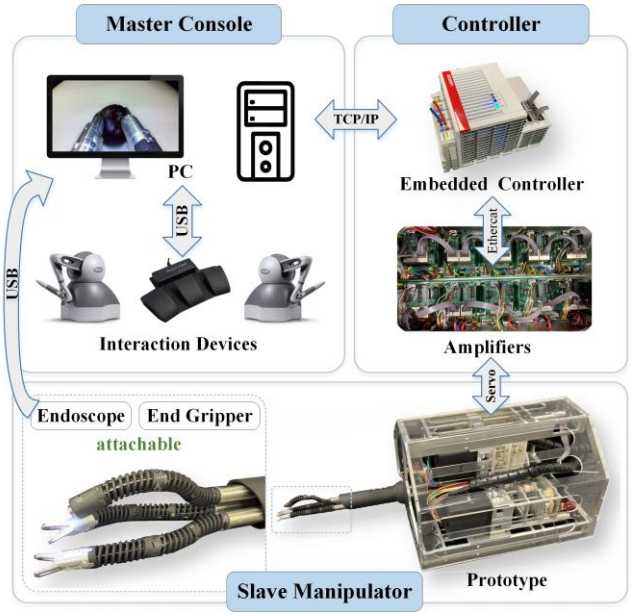

Fig. 6. The detailed control scheme and hardware configuration of the proposed TEM robotic system.

The hardware configuration of the proposed TEM robotic system has been designed and prototyped, as shown in Fig. 6. This robot-assisted surgical system adopts the master-slave control mode. At the master site, three interaction equipment consisting of two commercial haptic devices (Phantom Omni, SensableInc, USA) and a foot interface (FS3-P, Attme, China) connect with the PC via the USB connection. The PC delivers the motion signals collected by the interaction devices to the embedded controller (CX-5140, Beckhoff, Germany) through a TCP/IP connection. The inverse kinematic solutions are sent to the servomotor amplifiers (Uservo-Flex, MotionG, China) via EtherCAT. The slave manipulator houses 19 DC motors (DC19s, Maxon, Switzerland) that are equipped with an optical encoder (ENX16) and a harmonic gearbox (100:1) each. The endoscope (WS-MM1, Wiserscope, China) equipped with the slave manipulator has an imaging resolution of 720P and communicates with the computer monitor via USB, which is responsible for providing visual feedback. With this master-slave architecture, the motions of the surgeon's hands and feet are mapped to the slave manipulator. To ensure real-time functioning, the control frequency is set to 1000 Hz. The proposed robotic system has implemented a proportional and isomerous teleoperation strategy, which has been detailedly presented in the Appendix. D.

TABLE III
THE POSITIONING ERROR VALUES OF THE PROPOSED CONTINUUM JOINT

	Average error (L=23mm)	Maximum error (L=23mm)	Average error (L=29mm)	Maximum error (L=29mm)	Average error (L=37.5mm)	Maximum error (L=37.5mm)
horizontal plane*	0.21mm (0.66%)	0.33mm (1.43%)	0.26mm (0.90%)	0.45mm (1.55%)	0.29mm (0.77%)	0.43mm (1.14%)
vertical plane*	0.25mm (1.09%)	0.44mm (1.91%)	0.32mm (1.10%)	0.53mm (1.83%)	0.33mm (0.88%)	0.67mm (1.79%)

* The values in parentheses represent the relative error accounting for the total length of the continuum joint.

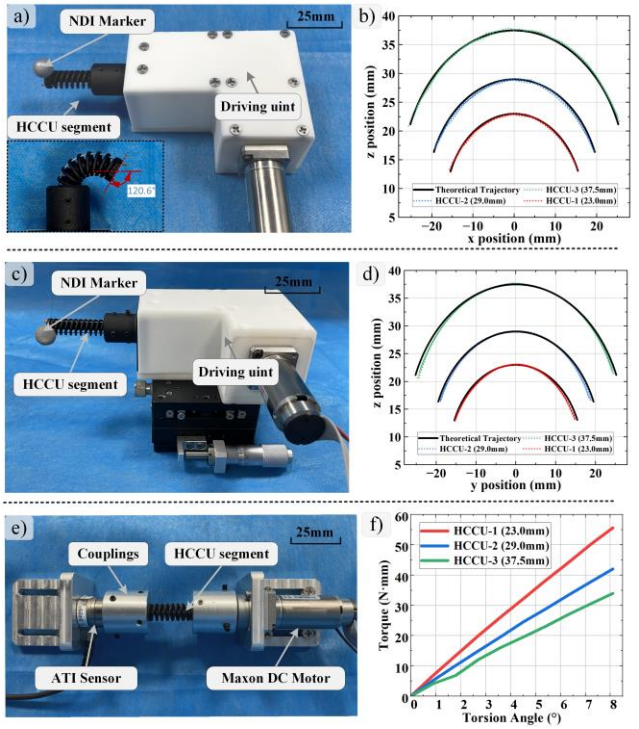

Fig. 7. a) Experimental setup for bending proformence of HCCU joints in the horizontal plane. b) Comparison for the theoretical trajectory and experimental results for the HCCU joint within ±100°. c) Experimental setup for bending proformence of HCCU joints in the vertical plane. d) Comparison for the theoretical trajectory and experimental results for vertical plane experimental within ±100°. e) Torsional stiffness experimental setup. f) Torque versus torsion angle for different HCCU.

B. Investigation on the Mechanical Properties of HCCU

1) Bending performances of the HCCU joint

The optimized HCCU joint with a length of 23 mm in the surgical instrument's continuum section and two additional HCCUs with 29 mm and 37.5 mm lengths were tested to investigate the constant curvature bending performances. The actual distal trajectories in the horizontal and vertical planes were recorded by an NDI optical tracking device (Polaris VEGA ST, Northern Digital Inc, Canada) and derived from three repeated tests, as shown in Fig. 7a) and c). The theoretical values were calculated by the kinematic model based on the constant curvature assumption, as shown in Fig. 7b) and d). The designed joint bent up to 120.6°, indicating that the HCCU features a large bending angle. The average and maximum position error values have been calculated and listed in Table III. The average end-positioning errors of the actual end trajectories in the horizontal and vertical planes within the range of [-100°, 100°] were both less than 0.33 mm, accounting for a relative error of 1.1% with respect to their total length. Besides, the maximum error values were both less than 0.67 mm, accounting for a relative error of 2.0%. The experimental results have demonstrated that the prototyped joints of varying lengths exhibit excellent constant curvature characteristics and possess an extensive bending range.

2) The anti-twisting property of the HCCU joint

The torsional performance of these three HCCU joints was experimentally investigated, and the experimental setup was illustrated in Fig. 7 e). The distal end of the designed HCCU joint was connected with a 6-axis force/torque sensor (Nano17, ATI Industrial Automation, USA) for twisting torque collection, and the proximal end was configured with a DC servomotor by a coupler. The motor generated a rotational motion with an interval step of 0.9° to drive the joints. The relationship between torque T and torsion angle φ has been plotted in Fig. 7f). The linear least square fitting method was utilized to calculate the torsional stiffness values of the three HCCUs. The results showed that the torsional stiffness values were 6.86 mNm/°, 5.19 mNm/°, and 4.66 mNm/°, respectively. It exhibits the high torsional stiffness of the single-segment HCCU, enhancing the stability and load capability of surgical instruments.

C. Positioning Accuracy for Trajectory Tracking of the Proposed Surgical Instrument in 3D Motions

To evaluate the overall positioning accuracy of the surgical instrument, the 2D circle trajectory and 3D spiral trajectory tracking experiments were carried out (Fig. 8). The surgical instrument was driven along the desired trajectories with different diameters according to the kinematic model based on the constant curvature assumption, as shown in Fig. 8 a1-a3). Meanwhile, the distal tip position values of this surgical instrument were recorded by the NDI optical tracking device, and the experimental results are shown in Fig. 8 b-e). For the circle trajectory tracking experiments, the average error values for these three experiments (with the circular diameters of 30mm, 40mm, and 50mm) are 1.11mm, 1.54mm, and 2.16mm respectively, accounting for 1.21%, 1.67%, and 2.35% of the length of this surgical instrument (92mm). In the two spiral trajectory tracking experiments, the average distal positioning error values are 3.17mm and 3.81mm respectively, accounting for 3.44% and 4.14% of the length of this surgical instrument. Both the circle and spiral trajectory tracking experiments require 3D motions of all three continuum segments, and the experimental results have validated the relatively high positioning accuracy of the proposed design.

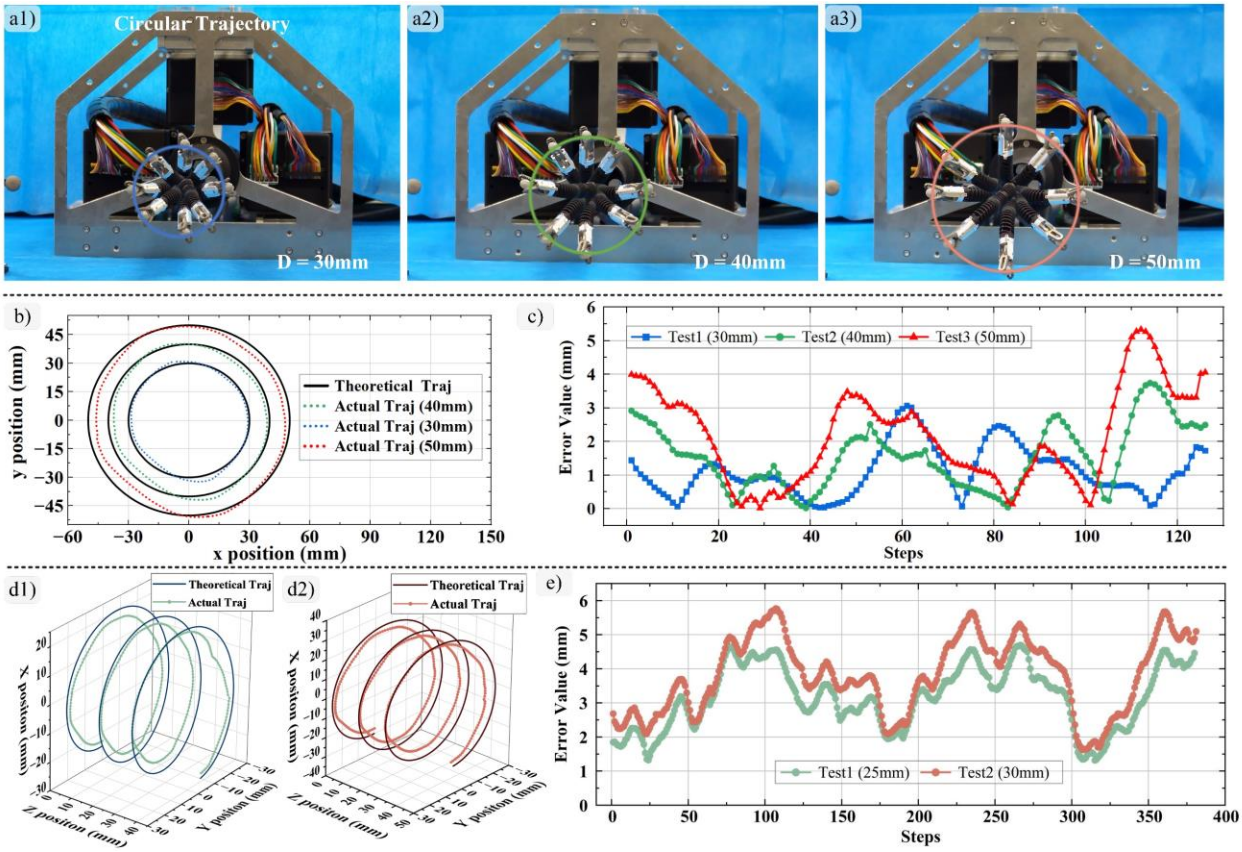

Fig. 8. a1-a3) The state of the surgical instrument as it traces circular trajectories with diameters of 30 mm, 40 mm, and 50 mm, respectively. b) Comparison for the theoretical trajectory and actual results and c) the absolute values of error of the 2D circle trajectory tracking experiments. d1-d2) Comparison for the theoretical trajectory and actual results and e) the absolute values of error of the 3D spiral trajectory tracking experiments.

D. Experiments for Payload Capability Investigation on the Surgical Instrument

The load capability of the surgical instrument has been investigated, and one optical maker has been mounted at the distal end to detect the deflection by the NDI optical measurement unit, as shown in Fig. 9 a1). One of the surgical instruments was selected and tested in four different configurations, which reflect various cases in a practical operational scenario, as shown in Fig. 9 b1). The standard weights with a step of 10 g were suspended on the distal end of the surgical instrument from 10 g to 150 g. The corresponding distal deflection values are recorded and depicted in Fig. 9 b2). The experimental values showed that the distal deflection of the continuum joint was within 20 mm under a 150 g payload. Due to the visual feedback in the master-slave control mode, the surgeon's hand-eye coordination can rectify the small distal deviation of less than 10% during minimally invasive surgery. Moreover, the surgical instruments achieved a maximum payload of 5N without causing structural collapse, as demonstrated in Fig. 9 a2). The results indicate that surgical instruments have the potential to perform high-load procedures such as suturing and knotting.

E. User Study Based on Training Exercises

The two typical training tasks/experiments that include string running (task 1) and circular peg transfer (task 2) have been performed for the user study. Four participants who are engineering students from Tianjin University conducted these training exercises on the proposed TEM robotic system. The participants were inexperienced in TEM surgery and lacked proficiency in operating surgical robots. During the string running task, users are required to manipulate the string to thread it through designated rings in a specific sequence and execute a wide-angle rotation, as shown in Fig. 9 c1). For the circular peg transfer exercise, users are required to operate the proposed robotic arms in a sequential manner to transfer both rings consecutively, as illustrated in Fig. 9 c2). The evaluation criteria form for these two tasks has been defined and will be filled out by the participants upon completion of the experiments, as presented in Table IV.

After obtaining participants' informed consent, they underwent experimental training that encompassed the following steps: 1) Acquiring knowledge of the motion mapping and operation methods of the proposed TEM robotic system in a master-slave control strategy; 2) Attaining proficiency in experimental protocols and regulations. Each participant completed four repetitions of each task and subsequently filled out a questionnaire. The duration of each task completion was recorded and presented in Fig. 10 a), and the user's operational process was incorporated into the uploaded multimedia materials. The experimental results indicate that the average completion times for the initial

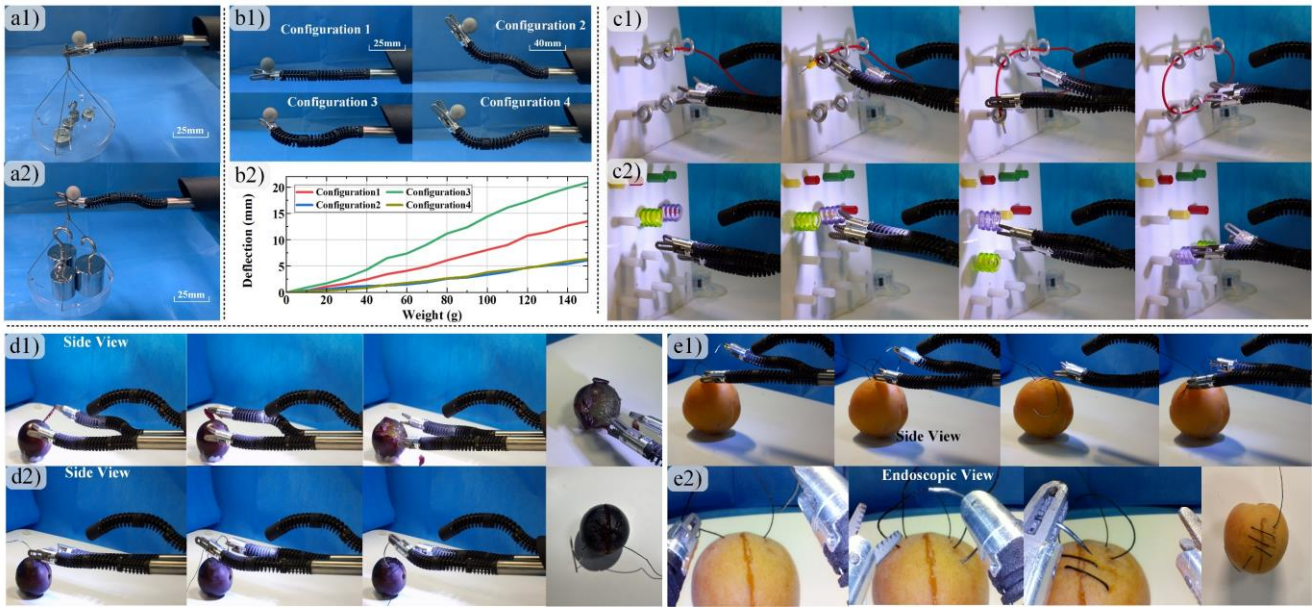

Fig. 9. a1) Small weights experiments setup. a2) Surgical instruments can withstand a maximum load of 5 N. b1) Different configurations of surgical instrument. b2) Deflections of the surgical instrument loaded by weights in different configurations. c1-c2) User trials tasks including string running and circular peg transfer. d1-d2) Surgical task simulation of grape peeling and grape suturing operations. e1-e2) Surgical task simulation of apricot suturing and threading operations.

TABLE IV
EVALUATION CRITERIA FORM FOR THE TWO TASKS

Item	Score	Statement
View Obstruction	1-10	Slight - Severe
Mental effort	1-10	Low - High
Operating difficulty	1-10	Easy - Difficult
Task difficulty	1-10	Easy - Difficult
Intuitiveness	1-10	Not intutitive -Intutitive
Operating Fatigue	1-10	Less - More

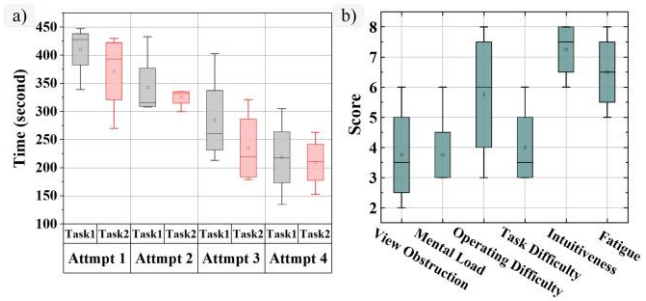

Fig. 10. a) The time taken to complete the tasks of string running (task 1) and circular peg transfer (task 2). b) Subjective evaluation of users on operating the proposed TEM robot to complete tasks.

attempts of both two tasks were 410.6 s and 371.8 s, respectively. However, with repeated practice and increased proficiency in operating the robot, these durations decreased to 218.8 s and 209.5 s on the fourth attempt, as illustrated in Fig. 10 b), which demonstrates the user-friendliness of the proposed TEM robot. Besides, the average scores for view obstruction, mental load, intuitiveness, and fatigue were 3.75, 3.75, 7.25, and 6.5 respectively. These results indicate that the proposed TEM robotic system exhibits intuitive hand-eye coordination and slight field-of-view occlusion, thereby facilitating user-friendly operation. However, users reported physical fatigue after prolonged operation, which may be attributed to the suboptimal ergonomics of the master console, and this issue will be refined by designing a specialized master arm in future iterations.

F. Surgical Task Simulations

Two surgical task simulations were carried out by two novices (majoring in engineering) to evaluate the operational flexibility and effectiveness of the proposed robotic system. These tasks included grape peeling and suturing operations as well as apricot suturing and threading operations, corresponding to simulating submucosal dissection and intraluminal suturing in TEM surgery, respectively. The detailed operational process has been illustrated in Fig. 9d1-e2), and these operations were also recorded and incorporated into the attached multimedia materials. Both sets of tasks were executed, and the average time durations to complete the two tasks were 200 s, 340 s, and 510 s, respectively. The experimental results demonstrate that the designed TEM robotic system has the potential to be utilized in TEM surgery with excellent maneuverability and an extensive surgical field of view.

G. Discussion

Specialized surgical robots increasingly tend to be developed to tackle TEM procedures in the narrow rectal environment, where the general-purpose robotic system cannot be addressed well. The investigation of the single HCCU unit and the trajectory tracking experiments that require motion coordination of the three continuum segments have been performed to validate the bending performance and the positioning accuracy. The user study experiments and the simulated operation tasks have been performed to demonstrate the usage potential for TEM procedures. Compared with the implementations [5] in ICL, the presented instrument not only has more DoFs but also has a deployable PACS segment, thus providing more intuitive hand-eye coordination and operational

triangulation. Compared with Shang's robot [14], the proposed robot has a 5-DoF endoscopic arm, which can be adjusted flexibly, significantly reduce visual field occlusion, and improve the user's operating experience. The integration of the distal continuum joint with the coated elastic sleeves made of biocompatible polyurethane and the sealing of the driving unit for surgical instruments will be performed to address the sterilization issue. The proposed modular tool design with rapid replaceability facilitates sterilization for different instruments. Moreover, fabricating the distal continuum section based on metal 3D printing will be investigated to further improve the fatigue resistance and loading capability of surgical instruments. The technical capabilities and performances of this robot and other single-port robots have been summarized in Table I in the Appendix. E.

V. Conclusion

This paper proposes a novel TEM robotic system that can enhance instrument triangulation and hand-eye coordination in narrow rectal scenarios while reducing the occlusion of view by introducing the HCCU unit and the modular multi-segment distal continuum section. A series of experiments have been conducted to validate the mechanical performance of the single-segment HCCU and the excellent maneuverability of the prototyped robotic system. The novel HCCU joint with 2 bending DoF achieves outstanding constant bending curvature characteristics and balanced stiffness. The multi-DoF continuum section based on the modular HCCU design can achieve the decoupling of position and orientation and simplifies the closed-form kinematic solution, providing an excellent example for the design of modular continuum joints. The proposed two-step design optimization method provides valuable guidance for designing surgical robots that operate in scenarios with narrow anatomical constraints, such as translaryngeal and transnasal surgery. Moreover, the proposed innovative HCCU joint and modular design concepts can be further applied to developing general single-port surgical robots. Future work will integrate the FBG-based distal force sensors [19], [20] to enhance feedback during operation.

References

[1] M. Araghi *et al.*, "Global trends in colorectal cancer mortality: projections to the year 2035," *Int. J. Cancer*, vol. 144, no. 12, pp. 2992–3000, 2019, doi: 10.1002/ijc.32055.

[2] P. Cr, "Transanal Endoscopic Microsurgery: Where it Stands as of Today?," *World J. Laparosc. Surg. DVD*, vol. 4, pp. 109–115, May 2011, doi: 10.5005/jp-journals-10007-1126.

[3] W. C. S. Meng, "Transanal Endoscopic Microsurgery (TEM)," in *Minimally Invasive Coloproctology: Advances in Techniques and Technology*, W. C. S. Meng, H. Y. S. Cheung, D. T. Y. Lam, and S. S. M. Ng, Eds., Cham: Springer International Publishing, 2015, pp. 91–101. doi: 10.1007/978-3-319-19698-5_11.

[4] M. H. Whiteford, "Local Excision of Rectal Neoplasia," in *The ASCRS Textbook of Colon and Rectal Surgery*, S. R. Steele, T. L. Hull, T. E. Read, T. J. Saclarides, A. J. Senagore, and C. B. Whitlow, Eds., Cham: Springer International Publishing, 2016, pp. 495–505. doi: 10.1007/978-3-319-25970-3_29.

[5] M. Covas Moschovas *et al.*, "Applications of the da Vinci single port (SP) robotic platform in urology: a systematic literature review," *Minerva Urol. Nephrol.*, vol. 73, no. 1, pp. 6–16, Feb. 2021, doi: 10.23736/s2724-6051.20.03899-0.

[6] M. Piccigallo *et al.*, "Design of a Novel Bimanual Robotic System for Single-Port Laparoscopy," *IEEEASME Trans. Mechatron.*, vol. 15, no. 6, pp. 871–878, 2010, doi: 10.1109/TMECH.2010.2078512.

[7] R. Yasin and N. Simaan, "Joint-level force sensing for indirect hybrid force/position control of continuum robots with friction," *Int. J. Robot. Res.*, vol. 40, no. 4–5, pp. 764–781, Apr. 2021, doi: 10.1177/0278364920979721.

[8] Y. Chen *et al.*, "The SHURUI System: A Modular Continuum Surgical Robotic Platform for Multiport, Hybrid-Port, and Single-Port Procedures," *IEEEASME Trans. Mechatron.*, pp. 1–12, 2021, doi: 10/gm6mn3.

[9] K. S. Roh, S. Yoon, Y. Do Kwon, Y. Shim, and Y.-J. Kim, "Single-Port Surgical Robot System with Flexible Surgical Instruments," in *Intelligent Robotics and Applications*, H. Liu, N. Kubota, X. Zhu, R. Dillmann, and D. Zhou, Eds., in Lecture Notes in Computer Science, vol. 9245. Cham: Springer International Publishing, 2015, pp. 447–459. doi: 10.1007/978-3-319-22876-1_38.

[10] Y. Chen, S. Zhang, Z. Wu, B. Yang, Q. Luo, and K. Xu, "Review of surgical robotic systems for keyhole and endoscopic procedures: state of the art and perspectives," *Front. Med.*, vol. 14, no. 4, pp. 382–403, Aug. 2020, doi: 10.1007/s11684-020-0781-x.

[11] J. Kim, M. de Mathelin, K. Ikuta, and D.-S. Kwon, "Advancement of Flexible Robot Technologies for Endoluminal Surgeries," *Proc. IEEE*, vol. 110, no. 7, pp. 909–931, Jul. 2022, doi: 10.1109/JPROC.2022.3170109.

[12] J. Shang *et al.*, "A Single-Port Robotic System for Transanal Microsurgery—Design and Validation," *IEEE Robot. Autom. Lett.*, vol. 2, no. 3, Art. no. 3, 2017, doi: 10.1109/LRA.2017.2668461.

[13] K. Leibrandt *et al.*, "Effective Manipulation in Confined Spaces of Highly Articulated Robotic Instruments for Single Access Surgery," *IEEE Robot. Autom. Lett.*, vol. 2, no. 3, Art. no. 3, Jul. 2017, doi: 10/gnbwp8.

[14] Y. Hu, W. Li, L. Zhang, and G.-Z. Yang, "Designing, Prototyping, and Testing a Flexible Suturing Robot for Transanal Endoscopic Microsurgery," *IEEE Robot. Autom. Lett.*, vol. 4, no. 2, Art. no. 2, Apr. 2019, doi: 10.1109/LRA.2019.2896883.

[15] X. Zhang, Y. Xian, Z. Cui, P. W. Y. Chiu, and Z. Li, "Design and modeling of a novel DNA-inspired helix-based continuum mechanism (DHCM)," *Mech. Mach. Theory*, vol. 171, p. 104702, May 2022, doi: 10/gn8bhw.

[16] H. Wang, X. Wang, W. Yang, Z. Du, and Z. Yan, "Construction of Controller Model of Notch Continuum Manipulator for Laryngeal Surgery Based on Hybrid Method," *IEEEASME Trans. Mechatron.*, vol. 26, no. 2, Art. no. 2, Apr. 2021, doi: 10/gn96m4.

[17] M. Russo *et al.*, "Continuum Robots: An Overview," *Adv. Intell. Syst.*, vol. 5, no. 5, p. 2200367, 2023, doi: 10.1002/aisy.202200367.

[18] D. A. Troncoso *et al.*, "A Continuum Robot for Remote Applications: From Industrial to Medical Surgery With Slender Continuum Robots," *IEEE Robot. Autom. Mag.*, pp. 2–13, 2022, doi: 10.1109/MRA.2022.3223220.

[19] Z. Tang, S. Wang, M. Li, and C. Shi, "Development of a Distal Tri-Axial Force Sensor for Minimally Invasive Surgical Palpation," *IEEE Trans. Med. Robot. Bionics*, vol. 4, no. 1, pp. 145–155, Feb. 2022, doi: 10.1109/TMRB.2022.3142361.

[20] Z. Dong *et al.*, "Shape Tracking and Feedback Control of Cardiac Catheter Using MRI-Guided Robotic Platform—Validation With Pulmonary Vein Isolation Simulator in MRI," *IEEE Trans. Robot.*, vol. 38, no. 5, pp. 2781–2798, Oct. 2022, doi: 10.1109/TRO.2022.3154691.